

Crystallization and stability of dysprosium iron garnet/Pt/gadolinium gallium garnet heterostructures on Si

Miela J. Gross¹, Jackson J. Bauer², Supriya Ghosh³, Kensuke Hayashi², Ethan R. Rosenberg², Andre K. Mkhoyan³, Caroline A. Ross²

¹Department of Electrical Engineering and Computer Science, Massachusetts Institute of Technology

²Department of Materials Science and Engineering, Massachusetts Institute of Technology

³Chemical Engineering and Materials Science, University of Minnesota

Abstract

The crystallization of rare earth iron garnet films such as dysprosium or europium iron garnet grown on Si substrates becomes increasingly challenging as the film thickness decreases. 50-75 nm thick dysprosium yttrium iron garnet (YDyIG) films without a seed layer are readily crystallized by a 750 °C rapid thermal anneal, forming a polycrystalline film with grains of several μm diameter containing radiating low-angle boundaries. The effect of Y:Dy ratio on the magnetization and anisotropy of DyIG is described. To crystallize thinner rare earth garnet films, bilayer stacks of a 50 nm thick paramagnetic gadolinium gallium garnet (GGG) seed layer and a 15 nm thick europium iron garnet (EuIG) film, and trilayer stacks consisting of a 50 nm thick GGG seed layer, a 1.5 nm thick Pt diffusion barrier and a 10 nm thick YDyIG film were prepared. The EuIG/GGG bilayers exhibit interdiffusion of Eu and Fe into the GGG. In contrast, the YDyIG/Pt/GGG trilayers exhibit agglomeration of the Pt leading to a morphology consisting of a polycrystalline garnet film enriched with Dy and Fe and containing a layer of Pt particles embedded near its surface.

Introduction:

Rare earth iron garnets ($\text{RE}_3\text{Fe}_5\text{O}_{12}$ or REIGs) are insulating ferrimagnets with magnetic characteristics that are beneficial for the development of spintronic and magnonic devices [1]–[5]. Rare earth substitution allows the magnetic properties such as saturation magnetization, magnetic anisotropy, compensation temperature, and Gilbert damping to be tuned [6]–[8]. The low damping found in $\text{Y}_3\text{Fe}_5\text{O}_{12}$ (YIG) and Bi-substituted YIG and the moderate damping of $\text{Tm}_3\text{Fe}_5\text{O}_{12}$ enable fast magnetization dynamics and domain wall motion [9]–[13]. Furthermore, perpendicular magnetic anisotropy (PMA) can be introduced into thin film REIGs via magnetoelastic anisotropy [14], [15] or growth-induced anisotropy [16]. Thin films with PMA are advantageous for studying domain walls and chiral spin textures [17], [18], which combined with their low damping makes REIGs attractive for applications in domain wall-based spin logic and memory devices [19], [20]. Furthermore, these insulating ferrimagnets restrict electrical pathways in device applications, reducing power dissipation [21].

For garnet-based spintronic devices to be compatible with CMOS technology, thin film REIG growth on silicon is necessary. There have been several demonstrations of polycrystalline garnet growth on non-garnet substrates, in particular Bi, Ce and Tb iron garnets for magneto-optical applications and Dy and Eu iron garnets with PMA, in which the garnets are typically grown by pulsed laser deposition or sputtering followed by annealing to crystallize the films [22], [23]. Some compositions including YIG and TbIG crystallize without a seedlayer, but in other cases, notably Ce and Bi-containing garnets, a YIG seedlayer is often needed to promote the formation of the garnet phase. Bauer et al. [8] showed that films of $\text{Dy}_3\text{Fe}_5\text{O}_{12}$ (DyIG) can be crystallized on silicon without a seedlayer for thicknesses of 22 nm and above, but thinner films did not crystallize under the same annealing conditions. The films exhibited PMA as a result of magnetoelastic anisotropy due to thermal mismatch strain as the film is cooled after the rapid thermal anneal (RTA). Dimensional scaling of devices and the importance of interfacial magnetic and exchange effects motivates the growth of sub-10 nm thick garnets on Si despite the difficulty in crystallizing thinner films. Aldossary et al. [24] showed epitaxial single crystalline YIG can be grown directly on 5 nm of Pt atop a $\text{Gd}_3\text{Ga}_5\text{O}_{12}$ (GGG) substrate. This drives our investigation of a tri-layer heterostructure of thin REIG/Pt/GGG/Si in which the GGG layer is intended to act as a virtual substrate, templating the crystallization of the REIG, and the Pt acts as a diffusion barrier.

In this article we report the thermal stability and microstructural development of heterostructures of 10 nm DyIG or Y-substituted DyIG ($\text{Y}_{1.5}\text{Dy}_{1.5}\text{Fe}_5\text{O}_{12}$, YDyIG)/1.5 nm of Pt/50 nm of GGG on Si, including the effect of Y in reducing the anisotropy and lowering the magnetic moment of DyIG. The Pt was grown at room temperature to suppress dewetting observed at 400 °C and above [25], whereas the garnet layers were grown at elevated temperatures, and the trilayer was finally crystallized by RTA. We describe the evolution of the microstructure including interdiffusion of the garnet layers and formation of Pt nanocrystals which led to a morphology of a polycrystalline garnet film containing a layer of subsurface Pt particles. This analysis of microstructural development gives insights to the stability of garnet/metal heterostructures that is relevant to integration of garnet-based spintronic devices on Si.

Methods

52 nm DyIG and 75 nm YDyIG polycrystalline single-layer films on Si were grown via pulsed laser deposition (PLD) from codeposition of stoichiometric DyIG and YIG targets. The laser used was a 248 nm KrF laser, with an energy of 350 mJ, a repetition rate of 10 Hz, and focused to a fluence of 2 J/cm² at the target. The chamber was pumped to a base pressure of 5 × 10⁻⁶ Torr and an oxygen pressure of 150 mTorr was maintained during the deposition. The substrates were heated to 650 °C at a ramp rate of 20 °C/min prior to deposition and cooled at the same rate post-deposition. The films underwent an *ex situ* rapid thermal anneal (RTA) at 750 °C for 5 minutes in oxygen using a MILA-5050 furnace. Additional samples of 15 nm $\text{Eu}_3\text{Fe}_5\text{O}_{12}$ (EuIG)/50 nm GGG bilayers were grown on Z-cut quartz substrates under similar deposition conditions and substrate temperature as the conditions used for the DyIG films. Two samples were made, one in which the GGG was grown, annealed *ex situ* by RTA then the EuIG was grown on top, and

the other in which the two layers were deposited sequentially and the bilayer was then annealed by RTA.

The DyIG/Pt/GGG and YDyIG/Pt/GGG heterostructures on silicon were grown in one chamber without breaking vacuum. First, 50 nm of GGG was deposited via PLD using a stoichiometric GGG target and the same deposition conditions as the DyIG and YDyIG films described above. After the chamber had cooled to < 60 °C and pumped to 5×10^{-6} Torr base pressure, 1.5nm of Pt was sputtered onto the samples in an argon pressure of 5 mTorr at 30 W from a Kurt J Lesker 5 cm diameter DC magnetron sputtering gun within the PLD chamber tilted 45° relative to the samples. Following sputtering, 10 nm of DyIG (or YDyIG) was deposited via PLD on the samples following the same process as for the 52 nm DyIG and 75 nm YDyIG films described above. The samples were then removed from the chamber for an *ex situ* RTA at 750 °C for 5 minutes.

Grazing incidence x-ray diffraction (GIXD) measurements were taken to analyze film crystallinity using a Rigaku Smartlab Multipurpose Diffractometer with a Cu $K\alpha$ x-ray source. Film thickness of the 52 nm and 75 nm thick DyIG and YDyIG films was determined with x-ray reflectivity performed on a Bruker D8 High Resolution Diffractometer. Hysteresis curves of the films were measured using a Digital Measurements Systems Vibrating Sample Magnetometer Model 1660 with field applied both in plane (IP) and out of plane (OP) of the substrate. Surface topography was investigated with a Bruker Icon Atomic Force Microscope (AFM) in tapping mode and Bruker RTESP-300 tips. In order to observe grain structure, electron backscatter diffractometry (EBSD) was carried out with Zeiss Merlin High-resolution scanning electron microscope (SEM). EBSD images were taken with the sample holder tilted at 70° with the electron beam set to an acceleration voltage of 15 kV at a working distance of 15 mm. The inverse pole figure (IPF) EBSD maps did not clearly resolve the grain shape, so image quality (IQ) EBSD maps [26], in which the contrast is derived from the change in orientation between neighboring scan steps, were used to characterize the grain shape.

Scanning transmission electron microscopy (STEM) imaging and energy dispersive X-ray (EDX) spectroscopy were used to characterize the structure and chemical composition of the heterostructures. Cross-sectional samples of the heterostructures were prepared using a focused ion beam (FIB) on a dual-beam FEI Helios Nanolab G4 FIB-SEM system. A 30 keV Ga ion beam was used to thin down the TEM lamella and finally a 2 keV ion-beam was used to remove damaged surface layers. The sample was coated with amorphous carbon prior to the sectioning to prevent damage to the surface on ion-beam exposure.

High angle annular dark-field (HAADF)-STEM imaging STEM-EDX elemental mapping was performed on an aberration-corrected FEI Titan G2 60-300 (S)TEM microscope equipped with a monochromator, CEOS DCOR probe corrector and super-X EDX spectrometer. The microscope was operated at 200 keV with a probe current of 80 pA. The HAADF images were collected with a probe convergence angle of 25.5 mrad and detector inner and outer collection angles of 55 and 200 mrad respectively.

Results

We first report the microstructure and properties of single layer 52 nm and 75 nm thick DyIG and YDyIG films grown directly on silicon and annealed. Grazing incidence X-ray diffraction (GIXD) of the 52nm DyIG/Si film is shown in Figure 1a. All peaks can be indexed to a polycrystalline garnet phase without detectable secondary phases. An AFM scan, Figure 1b, shows grains roughly 3 μm in diameter, consistent with our earlier work on similar films [8]. The YDyIG films similarly exhibit only garnet peaks when annealed.

Hysteresis loops for 52 nm DyIG on Si, Figure 1c, show an out of plane easy axis, saturation magnetization (M_s) of 30 kA m^{-1} , and coercivity $\mu_0 H_c = 300$ mT. The in-plane hysteresis loop displays an anisotropy field of $\mu_0 H_K = 750$ mT. The PMA is attributed to thermal mismatch strain as discussed previously [8]. On cooling from the annealing temperature, the DyIG thermal contraction is greater than that of Si, leaving the DyIG in IP tension. Both magnetostriction coefficients λ_{100} and λ_{111} of bulk DyIG are negative leading to a predicted negative magnetostriction coefficient for polycrystalline DyIG of $\lambda_s = -8.54 \times 10^{-6}$ [27]. From the analysis in [8] and the thermal expansion coefficients of the silicon substrate [28] and the garnet [29] a magnetoelastic anisotropy of 12.9 kJ m^{-3} is expected on cooling. This is sufficient to overcome the shape anisotropy ($\mu_0 M_s^2/2$ [30]) of 565 J m^{-3} yielding a film with PMA. An estimate of anisotropy field $H_K = 2K/\mu_0 M_s$ where K is the total anisotropy gives $\mu_0 H_K = 820$ mT, in reasonable agreement with the measured anisotropy field.

Y was substituted for Dy as $\text{Y}_x\text{Dy}_{3-x}\text{Fe}_5\text{O}_{12}$ in order to modify the anisotropy, coercivity and magnetization of the DyIG films on Si. Substitution of Y is expected to lower the dodecahedral sublattice moment, hence lowering the compensation temperature (= 220 K for bulk DyIG [31], [32]) and raising the room temperature M_s . Y substitution also lowers the magnetostriction coefficient and hence the magnetoelastic anisotropy [27]. A molecular field coefficient model [33] was used to calculate the compensation temperature and the room temperature M_s of $\text{Y}_x\text{Dy}_{3-x}\text{Fe}_5\text{O}_{12}$, Figure 2. This prediction is compared with experimental results from the room temperature out of plane (OP) hysteresis curves of 75nm thick $\text{Y}_x\text{Dy}_{3-x}\text{Fe}_5\text{O}_{12}$ films with five different Y:Dy ratios (Figure 1d). As the Y fraction increases, M_s increases from 30 to 140 kA m^{-1} , coercivity $\mu_0 H_c$ decreases from 250 mT to < 1 mT, and the PMA is reduced, with Y-rich films exhibiting an IP easy axis dominated by shape anisotropy. The experimental room temperature M_s values follow the trend of the MFC model but are consistently lower in magnitude which may indicate incompletely crystallized regions within the film.

The foregoing results show that for this film thickness range (52 – 75 nm) and annealing conditions (750 $^\circ\text{C}$, 5 min), DyIG and YDyIG crystallize as single phase garnet on Si without requiring a seed layer. However, earlier work [8] showed that DyIG films below 22 nm thickness grown on Si did not crystallize under the same annealing conditions. To promote the crystallization of thinner magnetic garnet films on Si, we therefore investigate the use of a seed layer of paramagnetic GGG. Figure 3 shows the results of annealing a bilayer of another garnet, EuIG, on a GGG seed layer. In Figure 3(a,b), 50 nm GGG seed layer is deposited and annealed by RTA, causing its crystallization into grains with ~ 100 nm in-plane dimensions. A 15 nm EuIG overlayer grown on the GGG and annealed forms a conformal layer, and elemental mapping shows that Eu and Fe penetrate throughout the GGG grain boundaries. In contrast, growing

GGG then EuIG sequentially followed by RTA yields a diffuse interface in which Eu and Fe are concentrated at the top of the film, but are also present within the GGG layer. These results inspire the use of a diffusion barrier to limit the interdiffusion between Gd and Dy, and between Ga and Fe.

To incorporate a diffusion barrier in addition to a seed layer, heterostructures of 10 nm DyIG/1.5 nm Pt/50 nm GGG and YDyIG($Y_{1.5}Dy_{1.5}Fe_5O_{12}$)/Pt/GGG were prepared. Figure 4 highlights the role of each layer of the DyIG/Pt/GGG heterostructure on the crystallization, assessed using GIXD. The bottom two scans show 10 nm of DyIG grown directly on Si and on Pt-coated Si. Without the GGG templating layer, no garnet peaks are visible from the 10 nm DyIG layer. In contrast, when the GGG templating layer is present, garnet peaks are observed, though it is not possible to distinguish the peaks of GGG from those of DyIG due to their close lattice match. Despite its crystallinity, the DyIG/GGG film showed no magnetic hysteresis, attributed to interdiffusion of the Fe and Dy into the GGG during annealing leading to a paramagnetic garnet. In contrast, annealed DyIG/Pt/GGG/Si and YDyIG/Pt/GGG/Si did show magnetic hysteresis, Figure 5. The OP loop of the DyIG/Pt/GGG/Si in Figure 5a had a coercivity of $\mu_0H_C = 40$ mT and $M_s = 17$ kA/m, which is smaller than that of thicker films of the same composition, 30 kA/m (Fig. 1c). In Figure 5b, YDyIG/Pt/GGG/Si showed an M_s of 100 kA/m, coercivity μ_0H_C less than 1 mT, and an IP easy axis. In both samples the magnetic characteristics appear consistent with the presence of a 10 nm thick DyIG or YDyIG layer, respectively, but further magnetic and microstructural analysis paints a more complex picture of the annealed trilayer garnet/Pt/garnet heterostructure.

To identify the origin of the magnetic signal, several partial film stacks were compared. Figure 5d shows VSM hysteresis loops of a sample of Pt/GGG/Si measured after 750 °C RTA. The effective magnetic signal (moment divided by the nominal volume of the DyIG film) is over an order of magnitude smaller compared to that of the DyIG/Pt/GGG/Si and $Y_{1.5}DyIG/Pt/GGG/Si$ films, indicating that the magnetism of the trilayer heterostructure comes from the magnetic garnet layer and not from other layers or the substrate. Figure 5c shows VSM of a DyIG/Pt/GGG/Si sample before RTA. The M_s of the unannealed film is similar to that of the annealed film but the loops indicate lower anisotropy. These results show that the DyIG contributes a magnetic signal even prior to RTA which may originate from partial crystallization during its growth at 650 °C. The GIXD, Figure 4, indicates a weak garnet peak as well as a Pt peak prior to RTA which supports the hypothesis of partial crystallization of the DyIG or GGG during growth.

The microstructure of the trilayer films after annealing at 750 °C was characterized using a combination of SEM, EBSD and HAADF-STEM imaging with spatial EDX maps. The top-view SEM images from the DyIG/Pt/GGG/Si stack (Figure 6a) show large circular regions about 50 μ m in size which appear to have nanocrystals embedded on the top surface, surrounded by smoother regions with finer features. To understand the garnet grain orientation in these regions, IPF-EBSD and IQ-EBSD maps were obtained, Figure 6b-e. While IPF-EBSD gives information on crystal orientation, the IQ-EBSD map shows diffraction intensity, which highlights grain boundaries and the grain structure. IQ-EBSD of the outer smoother region, Figure 6e, shows

garnet grains roughly 1-3 μm in diameter, each with a radiating pattern of lines resembling that seen in the grains of YIG and DyIG films [8], [9]. The line patterns are believed to originate from instability of the growth front as the grains grow into the amorphous region, but the crystal orientation on either side of the radiating lines is almost identical. The straight grain boundaries indicate that the grains nucleated simultaneously and grew to impingement. Figures 6b-c show IPF-EBSD and IQ-EBSD maps from the circular granular region. The region shares a common orientation despite the presence of radiating lines, indicating it is a large garnet grain formed by secondary grain growth. We hypothesize that the secondary grain growth occurs during the final 750 $^{\circ}\text{C}$ RTA step.

HAADF-STEM cross-sectional imaging of both DyIG/Pt/GGG and YDyIG/Pt/GGG shows that the garnet layers were polycrystalline with nanoparticles embedded near the top surface. The YDyIG/Pt/GGG showed multiple vertical grain boundaries, Figure 7 and Figure S1. Most of the boundaries are low angle, according to Fast Fourier Transforms (FFTs) of the atomic resolution HAADF images. This is in good agreement with the EBSD orientation maps shown in Figure 6, where radiating line patterns are visible within individual grains. A few of the grain boundaries are high angle, and spaced on the order of μm apart. This is consistent with the model that the garnet film consists of 1-3 μm grains but within the grains, radiating linear features correspond to low angle grain boundaries. STEM-EDX maps show that the nanocrystals of about 13 nm diameter at the top surface are predominantly Pt, indicating that dewetting occurs during the synthesis of the heterostructure. No distinct YDyIG layer was observed near the top surface, though Fe, Dy, and Y were detected throughout the GGG layer, attributed to diffusion of the Fe and Dy ions into the GGG layer during growth and annealing (see Figure S2).

The DyIG/Pt/GGG/Si heterostructure showed a similar morphology of Pt nanocrystals atop a 50 nm crystalline garnet film. STEM-EDX maps show that the top ~ 10 nm of the garnet layer is rich in Dy and Fe. SEM (Figure 6) shows Pt nanocrystals about 25 nm in size on the top surface. In addition, some regions of darker contrast are visible in the HAADF-STEM images of the GGG garnet layer (Figure 7c and d), which correspond to higher concentrations of Fe and Dy as seen in the STEM-EDX maps (also see Figure S3).

From the STEM analysis, it is evident in both samples that the Pt layer undergoes a dewetting process either during the high temperature growth of the top DyIG garnet at 650 $^{\circ}\text{C}$ or during the RTA at 750 $^{\circ}\text{C}$, causing the Pt to migrate to the top surface [25]. By comparing the GIXD scans of DyIG/Pt/GGG/Si film before and after RTA, Figure 4, the Pt (111) peak becomes more intense and narrower after RTA, suggesting that agglomeration of the Pt occurred during RTA despite DyIG encapsulating the Pt layer. To investigate the effects a top garnet layer has on dewetting of Pt, 42nm of YDyIG was grown on 1.5nm of Pt on silicon and then annealed at 750 $^{\circ}\text{C}$ for 5 minutes. An SEM top surface image, Figure 8, indicates that dewetting occurs despite the 42 nm thick oxide layer covering the Pt, i.e the encapsulating garnet layer over the Pt does not prevent agglomeration.

To further clarify the microstructural evolution of the Pt, AFM images were taken at several stages of processing of DyIG/Pt/GGG/Si stacks, Figure 9. The surface of 50 nm thick GGG grown

at 650 °C on Si before and after RTA at 750 °C for 5 min is shown in Figures 9a and b. The roughness R_a decreased from 1.1 nm as grown to 0.3 nm after RTA, indicating that the GGG becomes smoother as it crystallizes. During growth of the trilayer stack, the Pt is deposited on unannealed GGG and the initial roughness, which is on the order of the Pt thickness, is expected to lead to a discontinuous Pt film. This Pt readily dewets on subsequent heating, since dewetting is promoted by thickness fluctuations or porosity [25]. Figure 9c shows 60 °C-deposited Pt/650 °C-deposited GGG/Si which has a surface roughness of 0.8 nm indicating that the as-grown Pt does not increase the roughness of the as-grown GGG. After RTA of the uncapped Pt/GGG/Si film, the Pt has dewetted into 50 – 100 nm-diameter islands, Figure 9d. Figures 9e and f shows images of the trilayer heterostructure DyIG/Pt/GGG/Si before and after RTA, in which RTA increases the roughness.

The data suggests that the discontinuous thin Pt which forms on the as-grown GGG layer is vulnerable to dewetting, which occurs primarily during the RTA of the full stack after the top layer of DyIG has been grown at 650 °C. Without the DyIG top layer, RTA generates large Pt particles (up to 100 nm) indicating a high Pt mobility at 750 °C. When the same process is applied to the trilayer, the DyIG top layer suppresses but does not prevent the agglomeration of the Pt and smaller particles are formed. The secondary grain growth in the garnet is associated with a coarsening of the Pt nanoparticles. The requirement of a 750 °C RTA to crystallize the as-grown garnet is therefore too high to maintain the integrity of the Pt layer, and its role as a diffusion barrier is compromised. Reducing the crystallization temperature of the garnet, smoothing the GGG seed layer, or using a more refractory metal as diffusion barrier, may allow the stack to be formed and crystallized without degrading the topography.

Conclusion

We have demonstrated the crystallization of DyIG and YDyIG films directly on a Si substrate using a rapid thermal anneal. Films of DyIG with thickness 52-75 nm crystallized as single-phase garnet on Si after RTA at 750 °C to form grains with diameters of several μm exhibiting radiating patterns consisting of low angle grain boundaries. The out of plane easy axis is a result of tensile strain in the DyIG film due to thermal expansion mismatch, with crystallization-induced densification likely also contributing to the strain state. Substitution of Y for Dy yields a series of films with decreasing coercivity and PMA and increasing magnetic moment at room temperature as expected from molecular field coefficient modeling, allowing the anisotropy and magnetic moment to be tuned over a wide range via composition control.

However, as the film thickness decreases, crystallization of the films into single-phase garnet is impeded. Growth and crystallization of bilayer EuIG/GGG illustrates significant interdiffusion between the two garnet layers prompting the inclusion of a Pt diffusion barrier. However, attempts to form 10 nm thick DyIG and YDyIG on Si by using a GGG seed layer/Pt diffusion barrier were unsuccessful as a result of dewetting of the embedded Pt layer to form metallic nanoparticles during RTA. Interdiffusion of the DyIG and GGG yields a diffuse interface. Although the magnetic moment of the DyIG/Pt/GGG and YDyIG/Pt/GGG are consistent with the nominally 10 nm thick Dy garnet layers, the presence of embedded Pt particles and the diffuse interface led to a low crystal quality of the thin Dy garnet. These results of garnet-metal

heterostructure growth and microstructural evolution are relevant for the development of materials for future spintronics applications.

Acknowledgements

The authors acknowledge support of SMART, one of seven centers in nCORE, a Semiconductor Research Corporation program, sponsored by the National Institute of Standards and Technology (NIST). CAR and JJB acknowledge support of NSF DMR 1808190. Part of this work was carried out in the shared experimental facilities of MIT's Center for Materials Science and Engineering, NSF DMR 1419807. The electron microscopy effort (S.G., K. A. M.) was supported by SMART. Parts of this work were carried out in the Characterization Facility, University of Minnesota, which receives partial support from the NSF through the MRSEC (Award Number DMR-2011401) and the NNCI (Award Number EECS-2025124) programs.

Figures

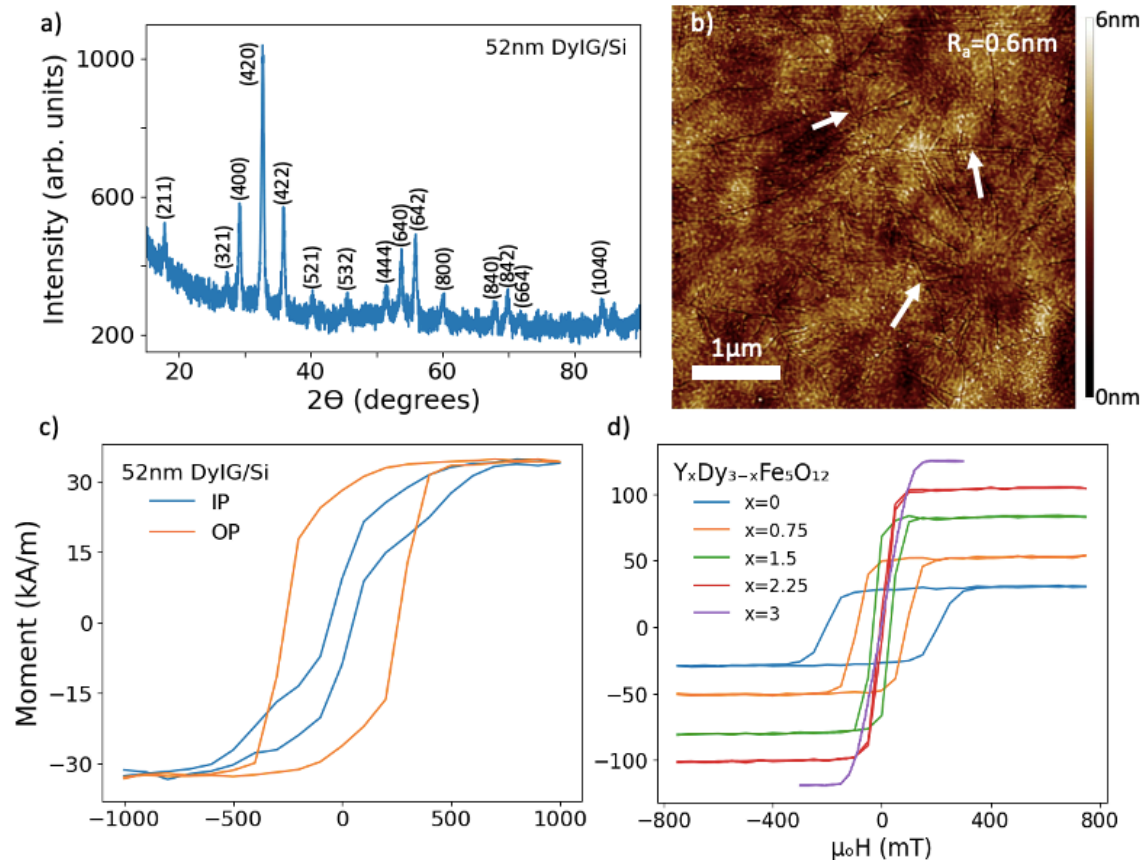


Figure 1. Characterization of 52nm DyIG/Si and 75nm thick YDyIG/Si. a) GIXD scan of DyIG/Si with peaks corresponding to single phase polycrystalline garnet. b) 5 μm by 5 μm AFM image of DyIG/Si surface that shows grains roughly 3 μm in size and grain boundaries indicated with arrows. The film has an average roughness of 0.6 nm. c) Hysteresis loops for IP and OP applied field for DyIG/Si, showing PMA. d) Hysteresis loops measured in the OP direction of YDyIG with composition $\text{Y}_x\text{Dy}_{3-x}\text{Fe}_5\text{O}_{12}$. [

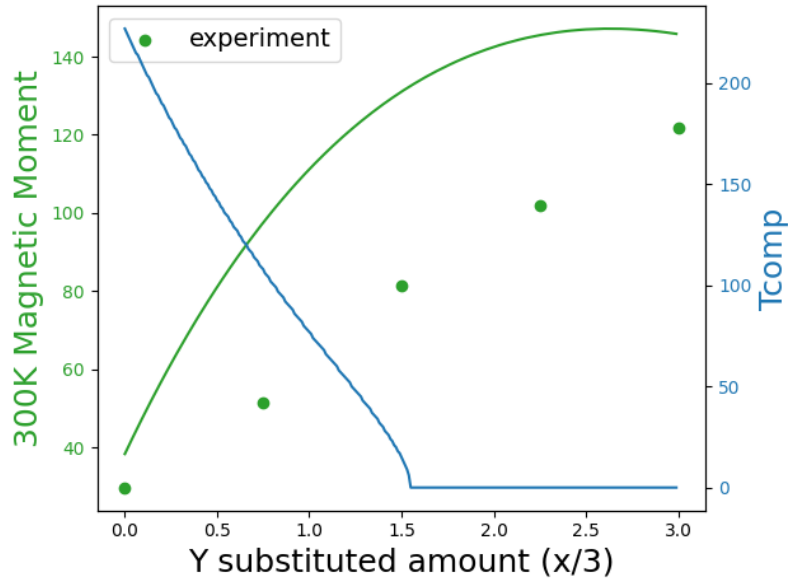


Figure 2: Saturation magnetization at 300K and compensation temperature as a function of Y content in $Y_xDy_{3-x}Fe_5O_{12}$. Points represent experimental data from Fig. 1(d).

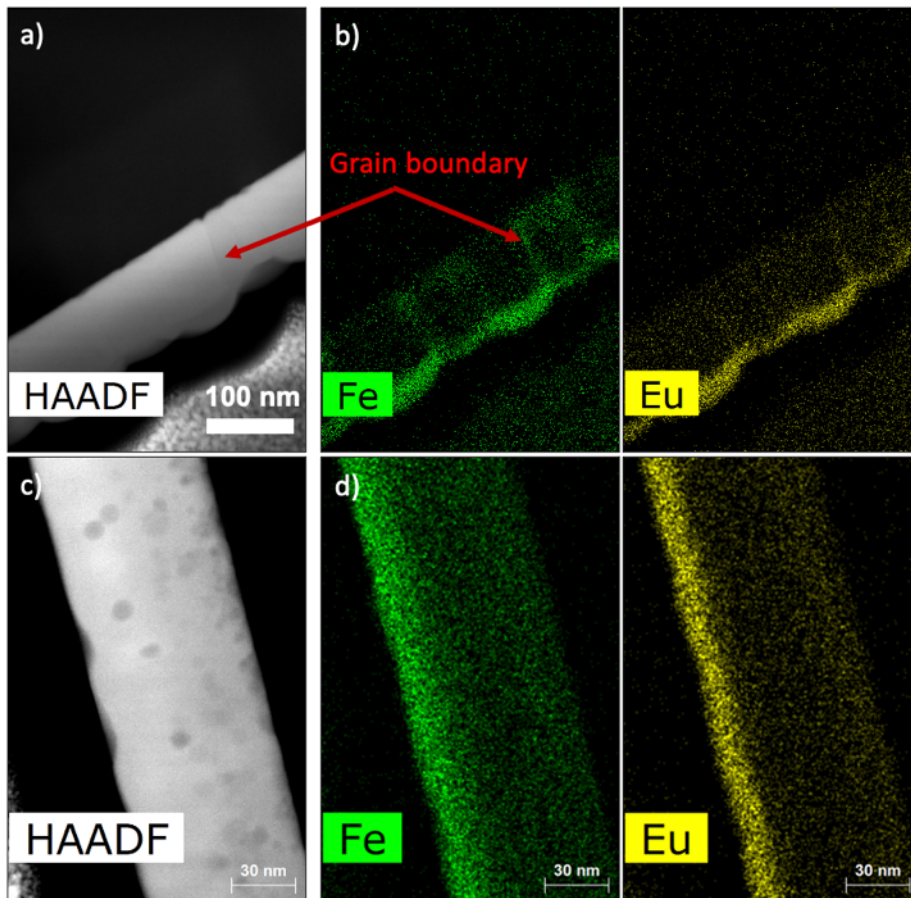


Figure 3: (a) HAADF-STEM image of EuIG/GGG/Si in which GGG was annealed before EuIG deposition. The arrow indicates a grain boundary. Scale bar is 100nm. (b) STEM-EDX compositional maps (in atomic %) for the Fe, and Eu. Diffusion of Fe into grain boundaries is

indicated with red arrows. (c) HAADF-STEM image of the EuIG/GGG/Si in which both layers were grown before the bilayer was annealed. Scale bar is 30 nm. (d) STEM-EDX compositional maps (in atomic %) shown for Fe and Eu.

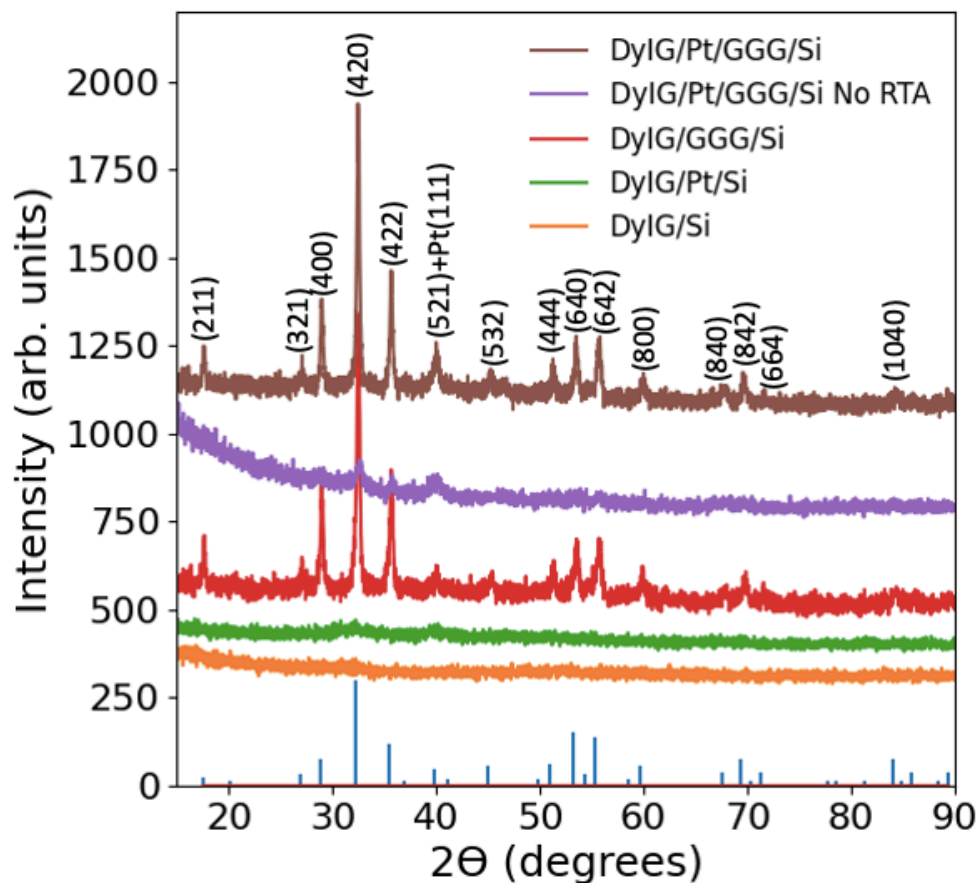


Figure 4: GIXD of the DyIG/Pt/GGG/Si heterostructure and partial film stacks after RTA unless otherwise indicated. Data has been vertically shifted for clarity and the powder diffraction peaks and intensities of garnet are marked on the horizontal axis.

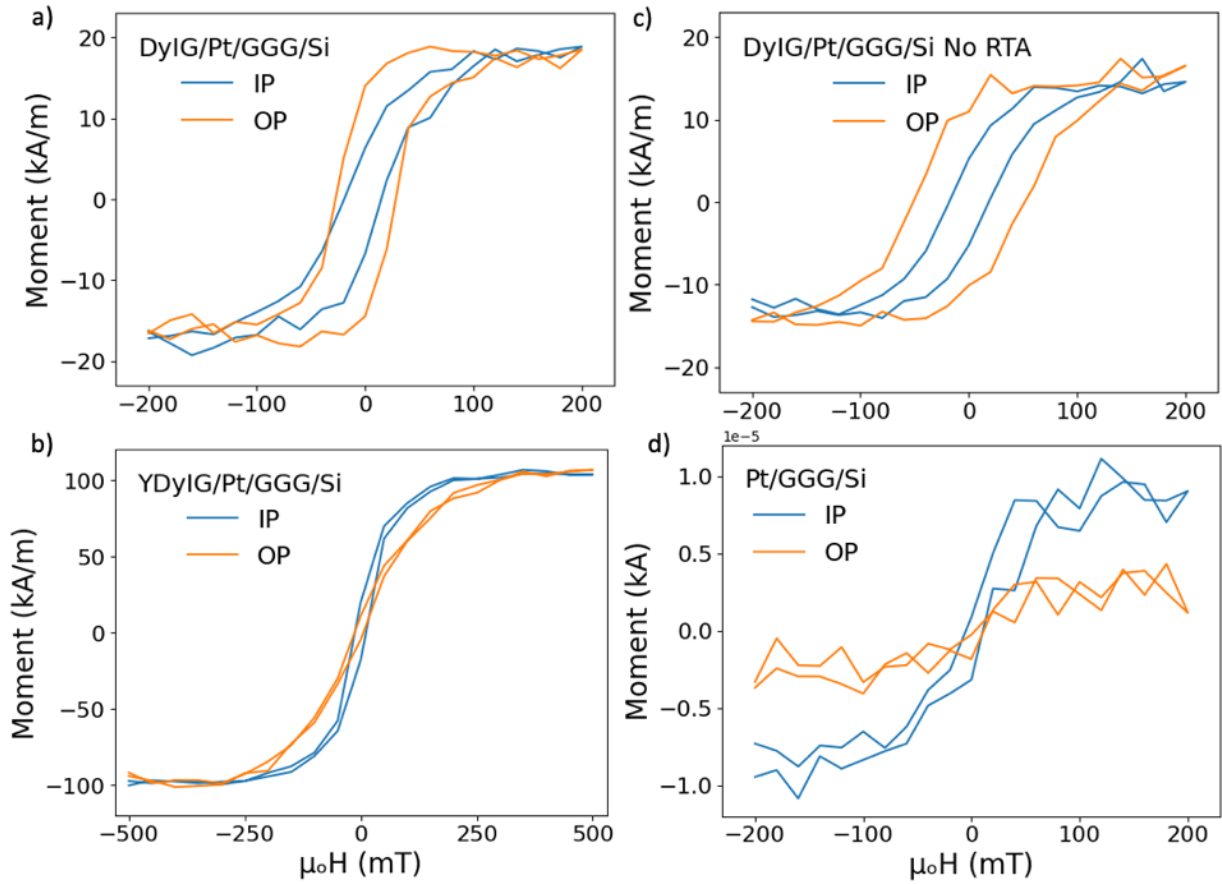


Figure 5: VSM hysteresis loops measured in IP and OP field directions of a) DyIG/Pt/GGG/Si after annealing, b) YDyIG/Pt/GGG/Si after annealing, c) DyIG/Pt/GGG/Si without RTA, and d) Pt/GGG/Si reference, showing negligible magnetic moment.

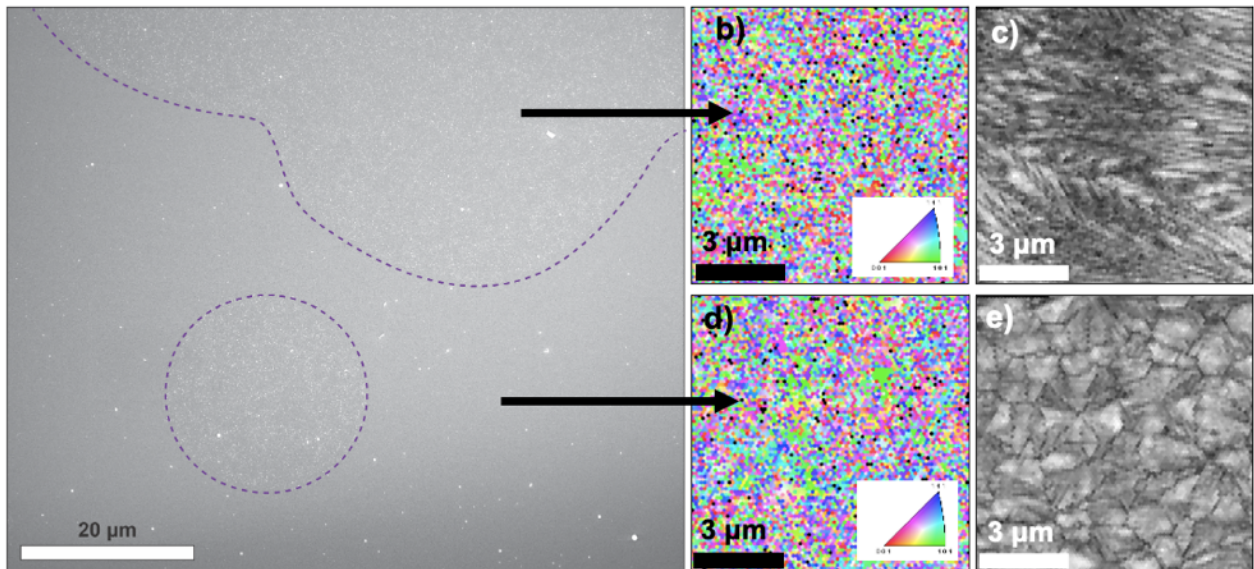


Figure 6: a) Top surface SEM image of DyIG(10nm)/Pt(1.5nm)/GGG(50nm)/Si. b-c) EBSD of circular region showing common orientation over 10 μm area. d-e) EBSD of area outside large

circular region showing 1-3 μm grains of garnet. b) and d) are inverse pole figure EBSD color maps showing zone axis of pixels, and c) and e) are image quality EBSD which is sensitive to changes in orientation between pixels. c) shows a large grain with radiating contrast and e) shows equiaxed grains.

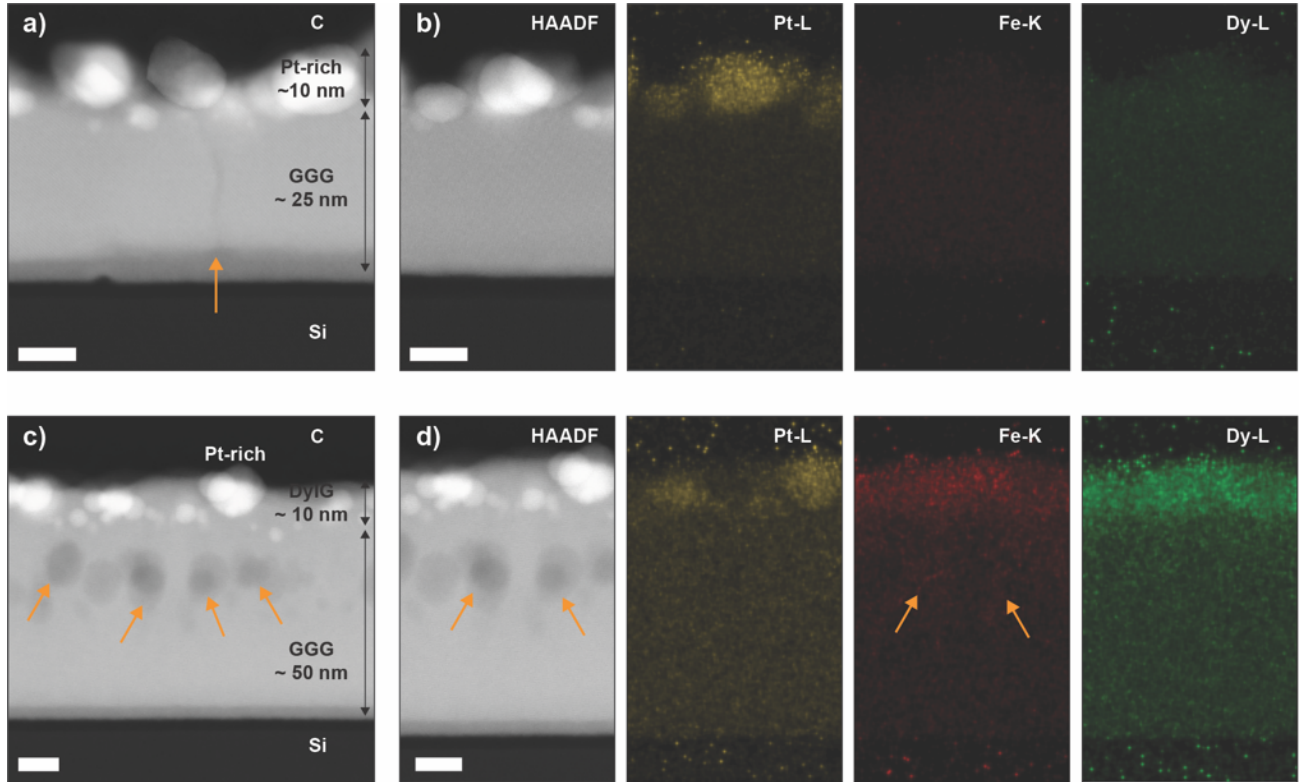


Figure 7: (a) HAADF-STEM image of the YDyIG/Pt/GGG/Si heterostructure. The arrow indicates a low-angle grain boundary. Scale bar is 10 nm. (b) STEM-EDX compositional maps (in atomic %) for the Pt, Fe, and Dy, indicating diffusion of the Fe and Dy into the GGG layer. Scale bar is 10nm. (c) HAADF-STEM image of the DyIG/Pt/GGG/Si heterostructure. Regions of darker contrast indicated by arrows are regions where Fe and Dy are at higher concentrations within the GGG layer. Scale bar is 10nm. (d) STEM-EDX compositional maps (in atomic %) shown for Pt, Fe, and Dy. A DyIG-rich layer is seen on top. Scale bar is 10nm.

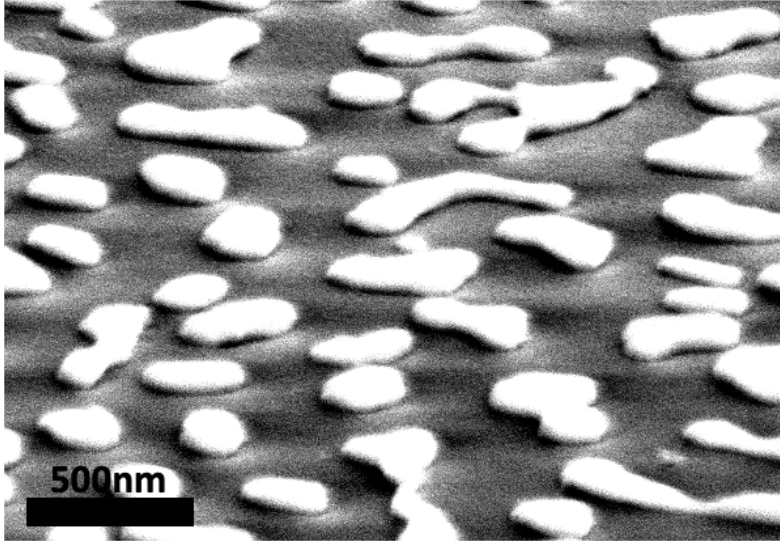


Figure 8: Top surface SEM of 42 nm Y-DyIG/1.5 nm Pt/Si after RTA at 750 °C.

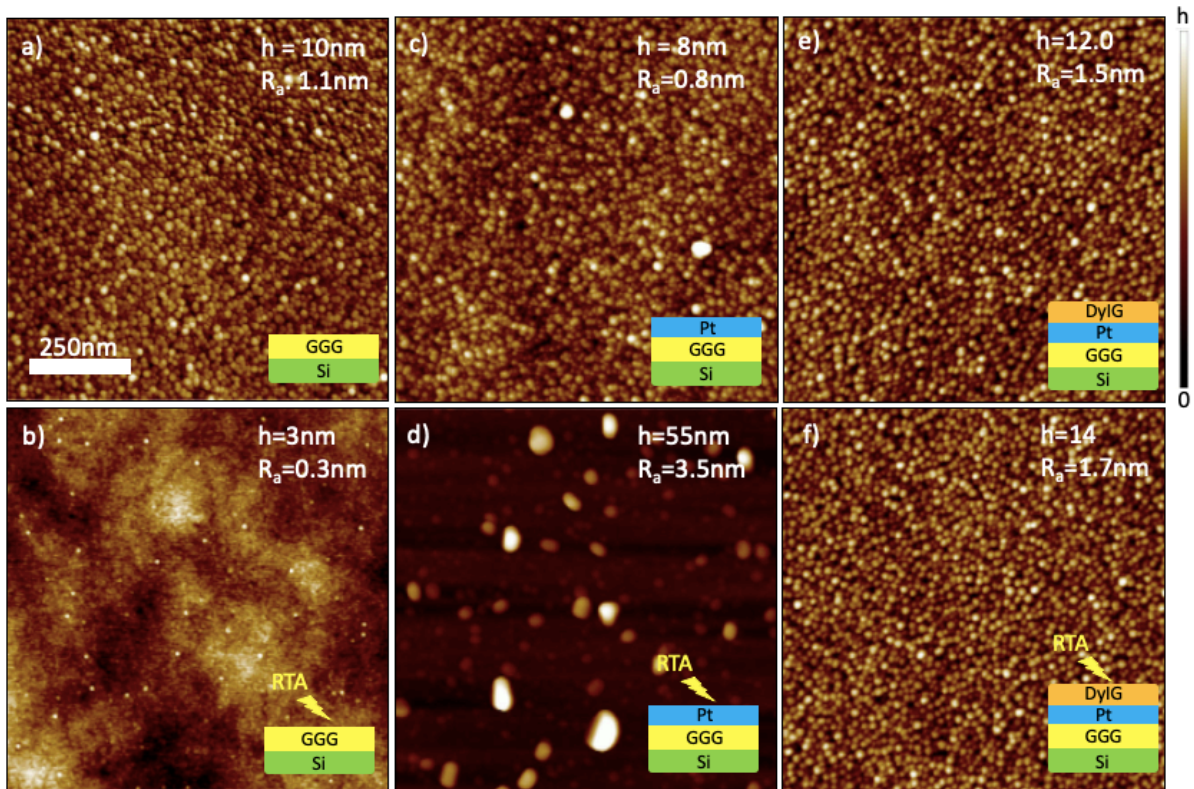


Figure 9: $1\mu\text{m}$ by $1\mu\text{m}$ AFM images of film stacks before and after annealing. a-b) 50 nm film of GGG/Si. c-d) (1.5nm)Pt/(50nm)GGG/Si. e-f) (10nm)DyIG/(1.5nm)Pt/(50nm)GGG/Si. a), c), and e) are as-grown and b), d), and f) are annealed at 750 °C for 5 minutes. h represents the vertical height range.

References

- [1] Y. Kajiwara *et al.*, “Transmission of electrical signals by spin-wave interconversion in a magnetic insulator,” *Nature*, vol. 464, no. 7286, pp. 262–266, 2010, doi: 10.1038/nature08876.
- [2] C. O. Avci *et al.*, “Current-induced switching in a magnetic insulator,” *Nat. Mater.*, vol. 16, no. 3, pp. 309–314, 2017, doi: 10.1038/nmat4812.
- [3] M. Montazeri *et al.*, “Magneto-optical investigation of spin-orbit torques in metallic and insulating magnetic heterostructures,” *Nat. Commun.*, vol. 6, pp. 1–9, 2015, doi: 10.1038/ncomms9958.
- [4] J. Chen *et al.*, “Strong Interlayer Magnon-Magnon Coupling in Magnetic Metal-Insulator Hybrid Nanostructures,” *Phys. Rev. Lett.*, vol. 120, no. 21, pp. 2–7, 2018, doi: 10.1103/PhysRevLett.120.217202.
- [5] L. J. Cornelissen, J. Liu, R. A. Duine, J. Ben Youssef, and B. J. Van Wees, “Long-distance transport of magnon spin information in a magnetic insulator at room temperature,” *Nat. Phys.*, vol. 11, no. 12, pp. 1022–1026, 2015, doi: 10.1038/nphys3465.
- [6] O. Ciubotariu, A. Semisalova, K. Lenz, and M. Albrecht, “Strain-induced perpendicular magnetic anisotropy and Gilbert damping of Tm₃Fe₅O₁₂ thin films,” *Sci. Rep.*, vol. 9, no. 1, pp. 1–8, 2019, doi: 10.1038/s41598-019-53255-6.
- [7] J. J. Bauer *et al.*, “Magnetic proximity effect in magnetic-insulator/heavy-metal heterostructures across the compensation temperature,” *Phys. Rev. B*, vol. 104, no. 9, pp. 1–9, 2021, doi: 10.1103/PhysRevB.104.094403.
- [8] J. J. Bauer *et al.*, “Dysprosium Iron Garnet Thin Films with Perpendicular Magnetic Anisotropy on Silicon,” *Adv. Electron. Mater.*, vol. 6, no. 1, pp. 6–13, 2020, doi: 10.1002/aelm.201900820.
- [9] T. Fakhrul, S. Tazlaru, L. Beran, Y. Zhang, M. Veis, and C. A. Ross, “Magneto-Optical Bi:YIG Films with High Figure of Merit for Nonreciprocal Photonics,” *Adv. Opt. Mater.*, vol. 7, no. 13, pp. 1–9, 2019, doi: 10.1002/adom.201900056.
- [10] H. Chang *et al.*, “Nanometer-Thick Yttrium Iron Garnet Films with Extremely Low Damping,” *IEEE Magn. Lett.*, vol. 5, 2014, doi: 10.1109/LMAG.2014.2350958.
- [11] C. O. Avci, A. Quindeau, M. Mann, C. F. Pai, C. A. Ross, and G. S. D. Beach, “Spin transport in as-grown and annealed thulium iron garnet/platinum bilayers with perpendicular magnetic anisotropy,” *Phys. Rev. B*, vol. 95, no. 11, Mar. 2017, doi: 10.1103/PhysRevB.95.115428.
- [12] C. Hauser *et al.*, “Yttrium Iron Garnet Thin Films with Very Low Damping Obtained by Recrystallization of Amorphous Material,” *Sci. Rep.*, vol. 6, 2016, doi: 10.1038/srep20827.
- [13] L. Caretta *et al.*, “Relativistic kinematics of a magnetic soliton,” *Science (80-.)*, vol. 370, no. 6523, pp. 1438–1442, 2020, doi: 10.1126/science.aba5555.
- [14] J. J. Bauer, E. R. Rosenberg, and C. A. Ross, “Perpendicular magnetic anisotropy and spin mixing conductance in polycrystalline europium iron garnet thin films,” *Appl. Phys. Lett.*, vol. 114, no. 5, 2019, doi: 10.1063/1.5074166.
- [15] R. F. Pearson, “Magnetocrystalline Anisotropy of Rare-Earth Iron Garnets,” *Proc. Seventh Conf. Magn. Mater.*, pp. 1236–1242, 1962, doi: 10.1007/978-1-4899-6391-8_87.
- [16] E. R. Rosenberg *et al.*, “Magnetic Properties and Growth-Induced Anisotropy in Yttrium Thulium Iron Garnet Thin Films,” *Adv. Electron. Mater.*, vol. 7, no. 10, pp. 1–11, 2021, doi: 10.1002/aelm.202100452.

- [17] C. O. Avci *et al.*, “Interface-driven chiral magnetism and current-driven domain walls in insulating magnetic garnets,” *Nat. Nanotechnol.*, vol. 14, no. 6, pp. 561–566, 2019, doi: 10.1038/s41565-019-0421-2.
- [18] F. Büttner *et al.*, “Thermal nucleation and high-resolution imaging of submicrometer magnetic bubbles in thin thulium iron garnet films with perpendicular anisotropy,” *Phys. Rev. Mater.*, vol. 4, no. 1, pp. 1–7, 2020, doi: 10.1103/PhysRevMaterials.4.011401.
- [19] A. Manchon *et al.*, “Current-induced spin-orbit torques in ferromagnetic and antiferromagnetic systems,” *Rev. Mod. Phys.*, vol. 91, no. 3, 2019, doi: 10.1103/RevModPhys.91.035004.
- [20] Y. Fan *et al.*, “Manipulation of Coupling and Magnon Transport in Magnetic Metal-Insulator Hybrid Structures,” *Phys. Rev. Appl.*, vol. 13, no. 6, pp. 1–6, 2020, doi: 10.1103/PhysRevApplied.13.061002.
- [21] M. Shalaby *et al.*, “Terahertz macrospin dynamics in insulating ferrimagnets,” *Phys. Rev. B - Condens. Matter Mater. Phys.*, vol. 88, no. 14, pp. 1–5, 2013, doi: 10.1103/PhysRevB.88.140301.
- [22] T. Goto, M. C. Onbaşlı, and C. A. Ross, “Magneto-optical properties of cerium substituted yttrium iron garnet films with reduced thermal budget for monolithic photonic integrated circuits,” *Opt. Express*, vol. 20, no. 27, 2012, doi: 10.1364/oe.20.028507.
- [23] N. Kumar, S. Prasad, D. S. Misra, N. Venkataramani, M. Bohra, and R. Krishnan, “The influence of substrate temperature and annealing on the properties of pulsed laser-deposited YIG films on fused quartz substrate,” *J. Magn. Magn. Mater.*, vol. 320, no. 18, 2008, doi: 10.1016/j.jmmm.2008.04.112.
- [24] M. Aldosary *et al.*, “Platinum/yttrium iron garnet inverted structures for spin current transport,” *Appl. Phys. Lett.*, vol. 108, no. 24, pp. 106–111, 2016, doi: 10.1063/1.4953454.
- [25] S. Strobel, C. Kirkendall, J. B. Chang, and K. K. Berggren, “Sub-10 nm structures on silicon by thermal dewetting of platinum,” *Nanotechnology*, vol. 21, no. 50, 2010, doi: 10.1088/0957-4484/21/50/505301.
- [26] X. Tao and A. Eades, “Alternatives to Image Quality (IQ) mapping in EBSD,” in *Microscopy and Microanalysis*, 2002, vol. 8, no. SUPPL. 2, doi: 10.1017/s1431927602106465.
- [27] S. Iida, “Magnetostriction Constants of Rare Earth Iron Garnets,” *J. Phys. Soc. Japan*, vol. 22, no. 10.1143/JPSJ.22.1201, pp. 1201–1209, 1967, [Online]. Available: <https://doi.org/10.1143/JPSJ.22.1201>.
- [28] Y. Okada and Y. Tokumaru, “Precise determination of lattice parameter and thermal expansion coefficient of silicon between 300 and 1500 K,” *J. Appl. Phys.*, vol. 56, no. 2, pp. 314–320, 1984, doi: 10.1063/1.333965.
- [29] S. Geller, G. P. Espinosa, and P. B. Crandall, “Thermal expansion of yttrium and gadolinium iron, gallium and aluminum garnets,” *J. Appl. Crystallogr.*, vol. 2, no. 2, pp. 86–88, 1969, doi: 10.1107/s0021889869006625.
- [30] B. D. Cullity and C. D. Graham, *Introduction to Magnetic Materials*. 2009.
- [31] S. Geller, J. P. Remeika, R. C. Sherwood, H. J. Williams, and G. P. Espinosa, “Magnetic study of the heavier rare-earth iron garnets,” *Phys. Rev.*, vol. 137, no. 3A, pp. 1034–1038, 1965, doi: 10.1103/PhysRev.137.A1034.

- [32] R. Pauthenet, "Magnetic properties of the rare earth pnictides," *J. Magn. Magn. Mater.*, vol. 8, no. 3, pp. 183–205, 1959, doi: 10.1016/0304-8853(78)90121-X.
- [33] G. F. Dionne, "Molecular field coefficients of substituted yttrium iron garnets," *J. Appl. Phys.*, vol. 41, no. 12, pp. 4874–4881, 1970, doi: 10.1063/1.1658555.

Crystallization and stability of dysprosium iron garnet/Pt/gadolinium gallium garnet heterostructures on Si

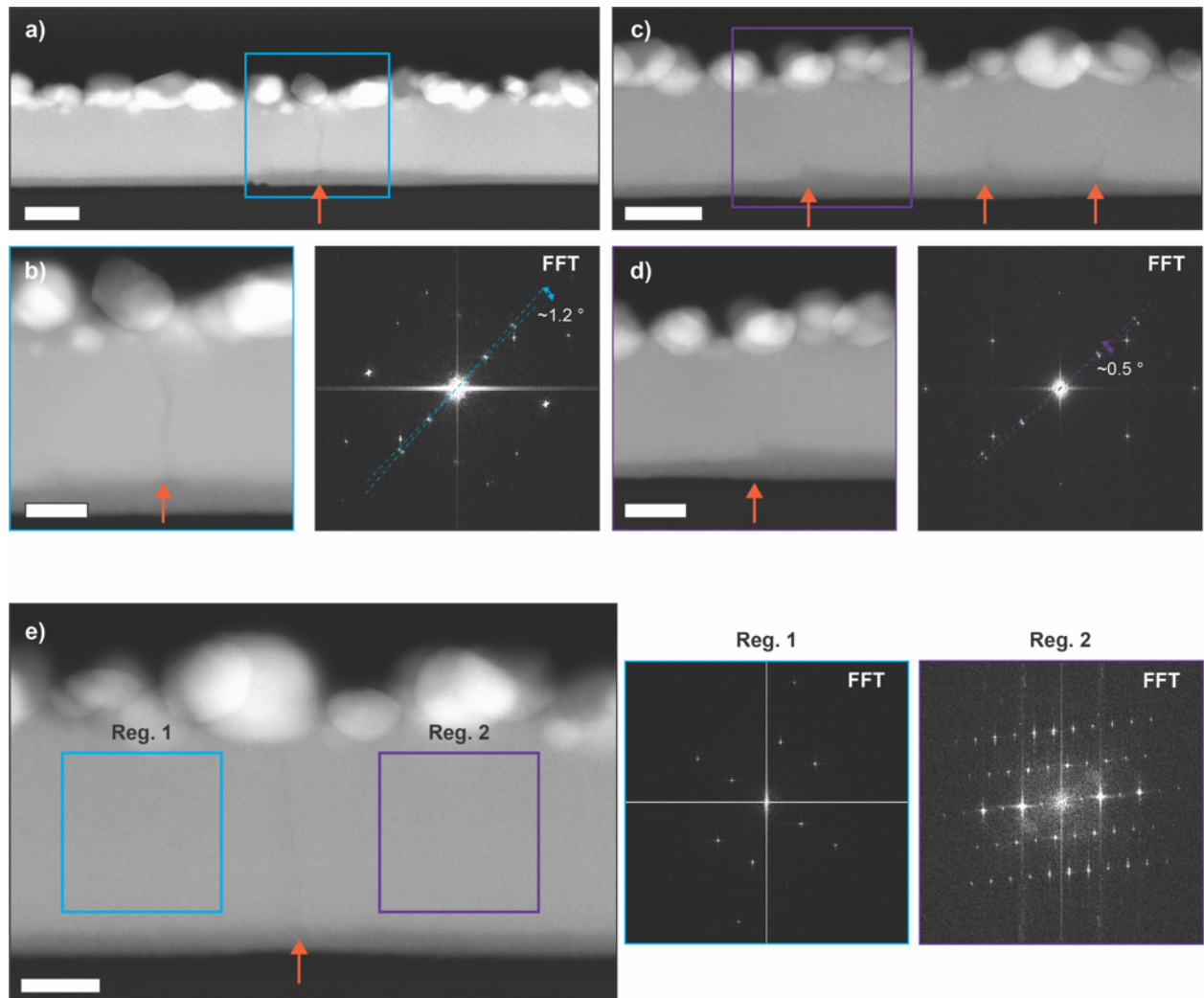
Miela J. Gross¹, Jackson J. Bauer², Supriya Ghosh³, Kensuke Hayashi², Ethan R. Rosenberg², Andre K. Mkhoyan³, Caroline A. Ross²

¹Department of Electrical Engineering and Computer Science, Massachusetts Institute of Technology

²Department of Materials Science and Engineering, Massachusetts Institute of Technology

³Chemical Engineering and Materials Science, University of Minnesota

Supplementary Information



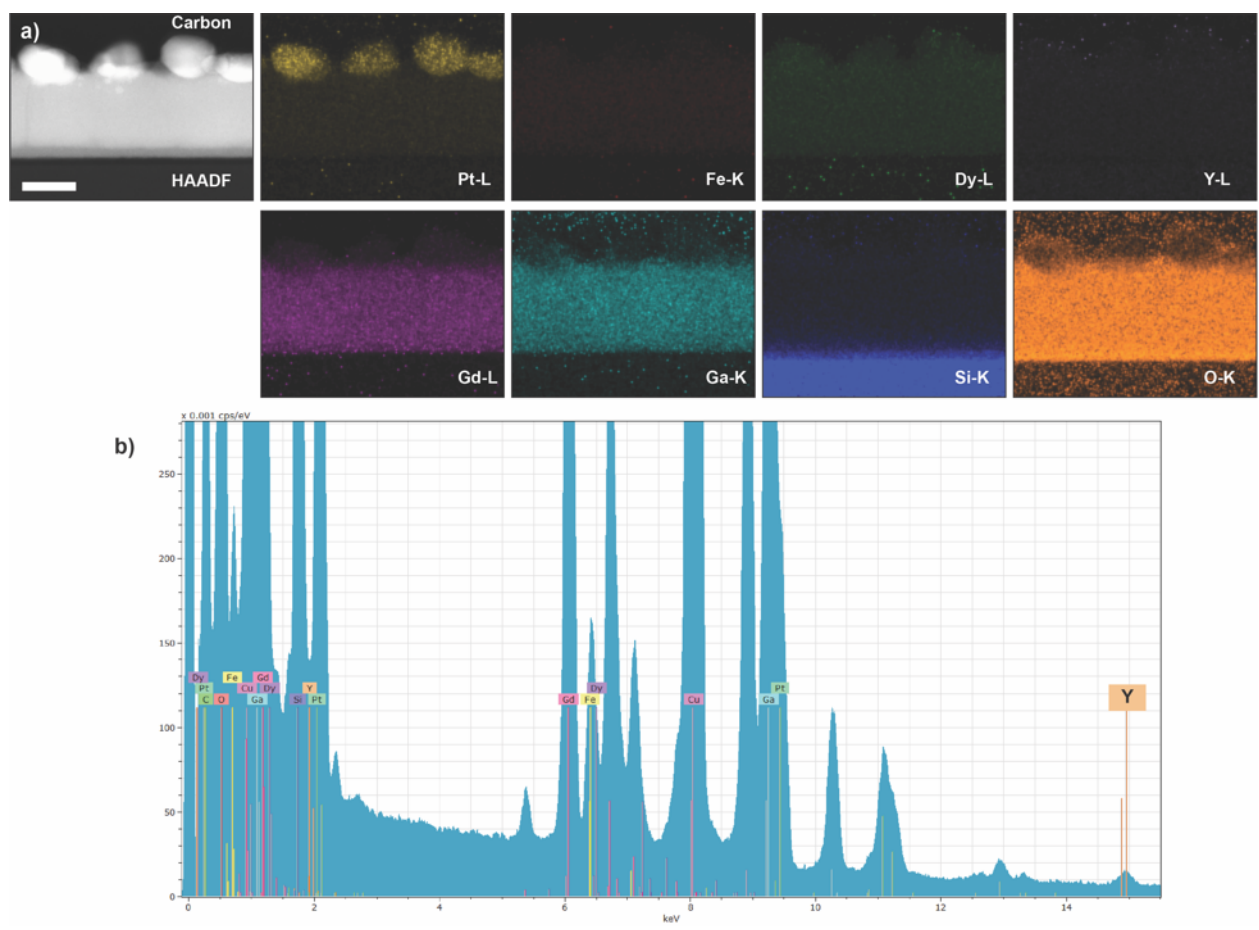


Figure S2: a) STEM-EDX maps from YDyIG/Pt/GGG/Si heterostructure for all elements. Signals from Y, Fe, and Dy are very weak; however, they are detected in the spectra shown in b). Scale bar is 20nm. b) EDX spectra from the film cross-sections with all elements present indicated. Note Cu and C signals originate from the Cu TEM grid and amorphous C coating.

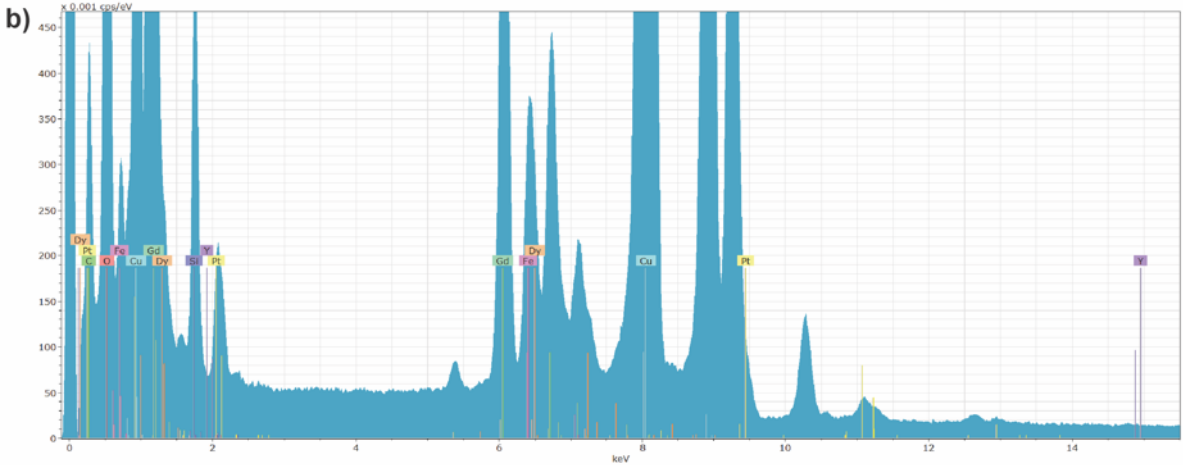
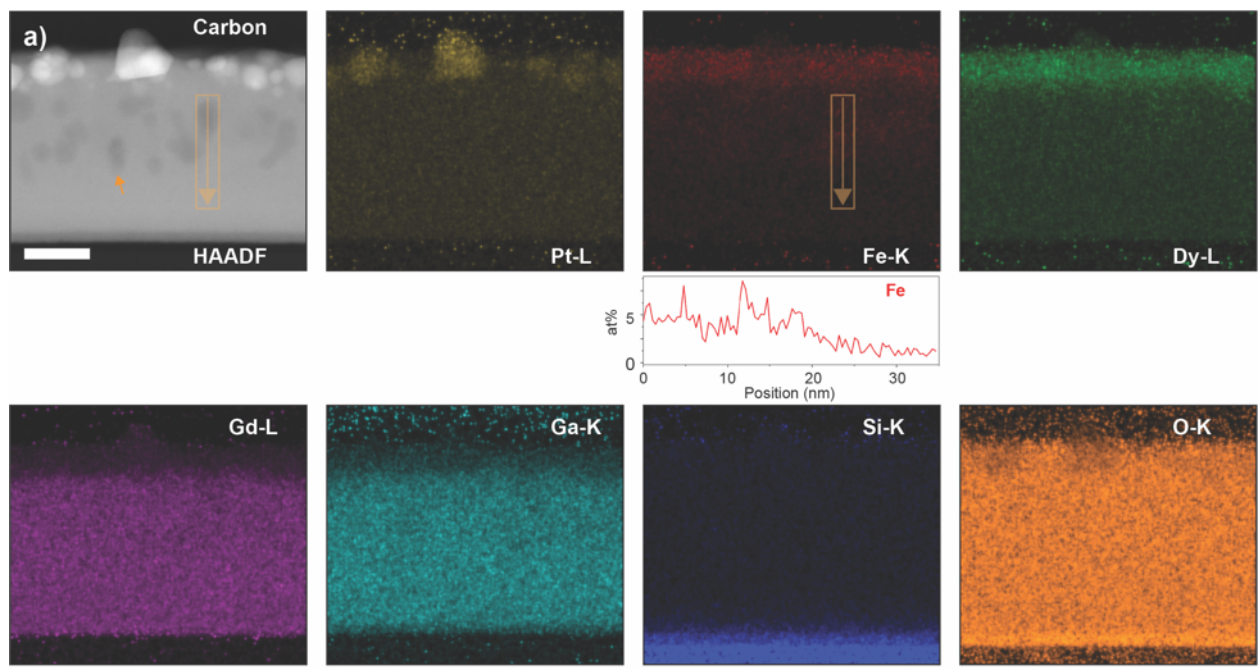


Figure S3: a) STEM-EDX maps from DyIG/Pt/GGG/Si heterostructure for all elements. Orange arrows point to regions of darker contrast in the HAADF images. Since Fe and Dy signals are higher in these regions, (see example line scan of Fe composition across the region), it can be argued that Fe and Dy atoms from the top DyIG layer have diffused out into the GGG layer. Scale bar is 20nm. b) EDX spectra from the film cross-sections with all elements present indicated. Note Cu and C signals originate from the Cu TEM grid and amorphous C coating.